Physics of the Earth and Planetary Interiors 219 (2013) 11–20

Contents lists available at SciVerse ScienceDirect

Physics of the Earth and Planetary Interiors

journal homepage: www.elsevier.com/locate/pepi

Separating intrinsic and apparent anisotropy

Andreas Fichtner[a,*], Brian L.N. Kennett[b], Jeannot Trampert[c]

[a] Department of Earth Sciences, Swiss Federal Institute of Technology, Zurich, Switzerland
[b] Research School of Earth Sciences, The Australian National University, Canberra, Australia
[c] Department of Earth Sciences, Utrecht University, Utrecht, The Netherlands

ARTICLE INFO

Article history:
Received 4 July 2012
Received in revised form 10 March 2013
Accepted 27 March 2013
Available online 6 April 2013
Edited by G. Helffrich

Keywords:
Seismic anisotropy
Apparent anisotropy
Intrinsic anisotropy
Seismic tomography
Mantle convection
Lattice-preferred orientation

ABSTRACT

Seismic anisotropy plays a key role in studies of the Earth's rheology and deformation because of its relation to flow-induced lattice-preferred orientation (LPO) of intrinsically anisotropic minerals. In addition to LPO, small-scale heterogeneity produces apparent anisotropy that need not be related to deformation in the same way as intrinsic anisotropy. Quantitative interpretations of observed anisotropy therefore require the separation of its intrinsic and apparent components.

We analyse the possibility to separate intrinsic and apparent anisotropy in media with hexagonal symmetry – typically used in surface wave tomography and SKS splitting studies. Our analysis is on the level of the wave equation, which makes it general and independent of specific data types or tomographic techniques.

We find that observed anisotropy can be explained by isotropic heterogeneity when elastic parameters take specific combinations of values. In practice, the uncertainties of inferred anisotropy are large enough to ensure that such a combination is always within the error bars. It follows that commonly observed anisotropy can always be explained completely by a purely isotropic laminated medium unless *all* anisotropic parameters are known with unrealistic accuracy. Most importantly, minute changes in the poorly constrained P wave anisotropy and the parameter η can switch between the possible or impossible existence of an isotropic equivalent.

Important implications of our study include: (1) Intrinsic anisotropy over tomographically resolved length scales is never strictly required when reasonable error bars for anisotropic parameters are taken into account. (2) Currently available seismic observables provide weak constraints on the relative contributions of intrinsic and apparent anisotropy. (3) Therefore, seismic observables alone are not sufficient to constrain the magnitude of mantle flow. (4) Quantitative interpretations of anisotropy in terms of mantle flow require combined seismic/geodynamic inversions, as well as the incorporation of additional data such as topography, gravity and scattered waves.

1. Introduction

Over the past few decades, work on seismic anisotropy has taken a prominent role in studies of the Earth because of the potential relation to geodynamic processes. In the field and in laboratory experiments, flow of geological materials leads to lattice-preferred orientations (LPO) of intrinsically anisotropic crystals, such as olivine in ophiolites. LPO produces materials with seismically observable anisotropy via the directional dependence of wavespeeds (e.g., Turner and peridotites, 1942; Verma, 1960; Hess, 1964; Zhang and Karato, 1996; Mainprice et al., 2005; Raterron et al., 2009). The consequence of such intrinsic seismic anisotropy is differences in wavespeed properties depending on polarisation: with shear-wave splitting in SKS waves accumulated along the path, and differences in the behaviour of Love and Rayleigh wave dispersion that cannot be explained by simple isotropic models. Analysis of observed seismic anisotropy has often concentrated on simple scenarios with nearly homogeneous media, so that all measures of observed seismic anisotropy represent model-based inferences rather than direct observations of material properties. The results have been taken up in geodynamic modelling, where observed seismic anisotropy – translated into Earth models via the solution of an inverse problem – has often been assumed to be entirely intrinsic, and thus represent a direct indicator of flow patterns (e.g., Ribe, 1989; Chastel and Dawson, 1993; Becker et al., 2006; Becker, 2008).

It was early recognised that many facets of observed seismic anisotropy can be mimicked by heterogeneous isotropic media, when the wavelengths employed are much larger than the scales of variation of the heterogeneity (e.g., Backus, 1962; Levshin and Ratnikova, 1984; Babuška and Cara, 1991; Fichtner and Igel,

* Corresponding author.
E-mail address: andreas.fichtner@erdw.ethz.ch (A. Fichtner).

0031-9201/$ - see front matter © 2013 Elsevier B.V. All rights reserved.
http://dx.doi.org/10.1016/j.pepi.2013.03.006

2008; Guillot et al., 2010; Capdeville et al., 2010a, in press). The shape-preferred orientation (SPO) of small fluid inclusions or cracks, for instance, can produce such apparent anisotropy (e.g., Babuška and Cara, 1991; Blackman and Kendall, 1997). Similarly, a finely stratified medium will appear transversely isotropic (equivalent to hexagonal crystal symmetry) and will display shear-wave birefringence with a separation of pulses of different polarisation. Consequently, observed anisotropy may be used to infer the presence of small-scale isotropic heterogeneity, including cracks (e.g., Crampin and Chastin, 2003) and melt pockets (e.g., Bastow et al., 2010).

The similarity of small-scale heterogeneity and large-scale anisotropy has profound consequences for seismic tomography that typically aims to find smooth models with as few parameters as possible. Small-scale structure that cannot be resolved by a finite amount of bandlimited data is suppressed from the outset via regularisation. This leads to tomographic models that are long-wavelength equivalents of potentially smaller-scale structure that cannot be resolved (Capdeville et al., in press). While regularisation is often a technical necessity, a smooth anisotropic model may also require less parameters or be statistically more plausible than a rough isotropic model that explains the data equally well (Montagner et al., 1988; Trampert and Woodhouse, 2003). This provides additional intuitive justification for this approach, because it seems in accord with Occam's razor, or the law of parsimony. While being useful formalisations of human intuition, neither statistics nor Occam's razor are fundamental laws of nature, and therefore unresolvable heterogeneity may map into large-scale apparent anisotropy. In surface wave tomography, for instance, the unknown details of crustal structure can produce apparent anisotropy in the mantle (Bozdağ and Trampert, 2008; Ferreira et al., 2010).

Evidence for structural heterogeneities capable of producing apparent anisotropy has grown rapidly, via sample analysis, studies of scattering, and seismic tomography. The Earth is undoubtedly heterogeneous on all scales with quasi-fractal behaviour over some scale ranges. Parts of this heterogeneity will appear as apparent anisotropy when interrogated by longer wavelength seismic waves. Furthermore, the heterogeneity itself will have been generated by geodynamic processes.

Thus, when we look at the interior of the Earth from the surface, we are faced with a situation where clear indications of anisotropy could arise from intrinsic effects such as LPO, or be apparent, representing averages through fine-scale heterogeneity – which itself could be anisotropic. To improve geodynamic understanding, we need to resolve the anisotropic components and, in particular, recognise the intrinsic component directly related to flow.

At the present time, the problem of separating intrinsic and apparent anisotropy is too complex in full generality. We can, however, examine simpler and illustrative problems. We here restrict attention to the case of transverse isotropy, where properties are symmetric about a preferred axis, equivalent to a crystal with hexagonal symmetry about this axis. We then ask if, given a set of transversely isotropic properties, do we need intrinsic anisotropy, or is there some equivalent combination of isotropic materials?

While it is well known that a small-scale isotropic model has a long-wavelength isotropic equivalent, the reverse problem considered here has, to the best of our knowledge, only been addressed by Backus (1962) – despite its outstanding geodynamic relevance. It is, a priori, not obvious which anisotropic models can be represented by an isotropic equivalent. The mere fact that one can go from any small-scale isotropic model to one anisotropic model does not imply that the opposite is true as well, i.e., that one can go from any anisotropic model to one small-scale isotropic model.

We will see that the solution to this problem is surprisingly complex, and that in many circumstances we cannot discriminate between intrinsic and apparent anisotropy. Where we can, the distinction depends on very precise controls on certain properties of the materials such as the P wavespeeds or the anisotropic parameter η that can hardly be determined from seismic observations.

This paper is organised as follows: following the definitions of apparent, intrinsic and observed anisotropy, we provide a brief review of the upscaling relations for finely layered media. We then discuss the set of inequalities that an anisotropic medium must satisfy to be representable by an equivalent finely layered isotropic medium. In Section 3.2, these inequalities are illustrated for the specific case of a vertical symmetry axis. A more detailed analysis in Section 4 confirms that small variations in elastic parameters can switch between existence and non-existence of isotropic equivalents. It follows, that isotropic equivalents can generally be found unless all elastic parameters are known with unrealistic accuracy. A detailed discussion of this result is provided in Section 6.

2. Structure-induced apparent anisotropy in layered media

To reduce the complexity of our analysis to a tractable level, we restrict ourselves to layered, transversely isotropic media described in terms of density and the elastic parameters a, c, f, l and n (Love, 1927). In this paragraph we briefly review the concept of structure-induced apparent anisotropy in layered media, as introduced by Backus (1962). This is intended to set the stage for subsequent developments. In the interest of a transparent terminology, we consider the case of a vertical symmetry axis. This allows us to use the notion of plane waves with horizontal or vertical polarisation and propagation directions. The formal development, however, applies to any orientation of the symmetry axis, including horizontal orientation relevant for the analysis of SKS splitting (e.g., Silver and Chan, 1988; Babuška and Cara, 1991).

We assume the stratified medium to vary appreciably over a length scale $\updownarrow$. When the wavelength is much longer than $\updownarrow$, wave propagation through the finely stratified medium is identical to wave propagation through a smoothed equivalent medium, the elastic parameters of which are given by the upscaling equations

$$A = \langle a - f^2 c^{-1} \rangle + \langle c^{-1} \rangle^{-1} \langle f c^{-1} \rangle^2, \quad C = \langle c^{-1} \rangle^{-1}, \quad F = \langle f c^{-1} \rangle \langle c^{-1} \rangle^{-1},$$
$$L = \langle l^{-1} \rangle^{-1}, \quad N = \langle n \rangle. \tag{1}$$

The symbol $\langle . \rangle$ represents the vertical average $\langle \phi \rangle (z) = \int w(\xi - z)\, \phi(\xi)\, d\xi$, where ϕ is any function, and the smoothing window w is required to be positive. The effective medium described in terms of A, C, F, L and N is referred to as a smooth, transversely isotropic, long-wavelength equivalent (STILWE). In the special case where the original layers are isotropic with $a = c = \lambda + 2\mu, f = \lambda$ and $l = n = \mu$, the effective parameters are given by

$$A = \langle 4\mu(\lambda+\mu)(\lambda+2\mu)^{-1} \rangle + \langle (\lambda+2\mu)^{-1} \rangle^{-1} \langle \lambda(\lambda+2\mu)^{-1} \rangle^2, C = \langle (\lambda+2\mu)^{-1} \rangle^{-1},$$
$$F = \langle (\lambda+2\mu)^{-1} \rangle^{-1} \langle \lambda(\lambda+2\mu)^{-1} \rangle, \quad L = \langle \mu^{-1} \rangle^{-1}, \quad N = \langle \mu \rangle. \tag{2}$$

Unless λ and μ are constant, we find $A \neq C$ and $L \neq N$, meaning that isotropic layering induces apparent anisotropy when wavelengths much longer than $\updownarrow$ are observed. This phenomenon is illustrated in Fig. 1.

Eqs. (1) and (2) gain special relevance in the context of structural inverse problems that are generally under-determined due to the finite amount of independent seismic data. Under-determinacy implies the need for regularisation, i.e., the enforcement of smoothness that prevents the appearance of small-scale features (e.g., fine layers) that cannot be resolved (e.g., Trampert et al., 2013). It follows that seismic inverse problems produce long-wavelength equivalents with at least some degree of apparent anisotropy – the only exception being the unlikely case where

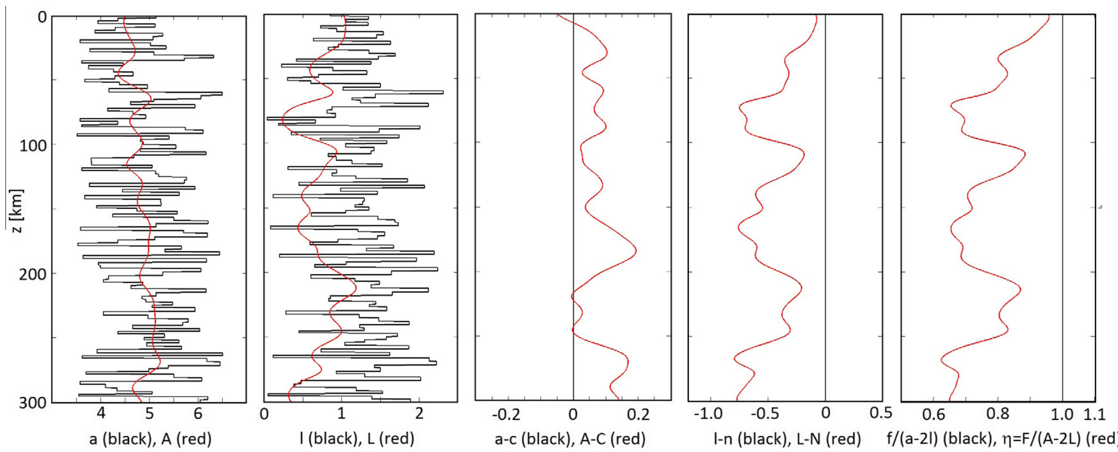

Fig. 1. Exemplary illustration of apparent anisotropy induced by long-wavelength equivalence. The original stratified medium, plotted in black, is strongly heterogeneous over length-scales of around 5 km, which is the average width of the layers. This medium is isotropic, i.e., $a - c = 0, l - n = 0$ and $f/(a - 2l) = 1$. Taking the averaging window $w(z)$ to be a Gaussian with half width 15 km, the upscaling Eqs. (1) provide the long-wavelength equivalent medium, plotted in red. As predicted by Eq. (2), the long-wavelength equivalent is anisotropic, with $A - C \neq 0, L - N \neq 0$ and $\eta = F/(A - 2L) \neq 1$ (e.g., Takeuchi and Saito, 1972). Seismic waves with wavelengths significantly larger than the averaging width of 15 km are identical when propagating through either the original (black) or the long-wavelength equivalent (red) medium.

the Earth is indeed homogeneous on length scales below the resolution length.

Any deformation state of the STILWE medium must have non-negative internal energy to ensure stability. This requirement is fulfilled, when the elastic coefficients satisfy the inequalities (Backus, 1962):

$$C \geqslant 0, \quad L \geqslant 0, \quad N \geqslant 0, \quad A - N \geqslant 0, \quad (A - N)C \geqslant F^2. \tag{3}$$

That the STILWE medium is indeed elastically stable follows from the substitution of (1) into (3).

3. The existence of finely layered isotropic equivalents

3.1. The Backus conditions

Equipped with the machinery from the previous section, we return to our original question: under which conditions is a smooth transversely isotropic medium equivalent to a finely layered isotropic medium?

Again following Backus (1962), we introduce a new set of elastic parameters that facilitates the subsequent analyses. Instead of L, N, A, C and F, we shall use L, N, R, S, and T, with

$$R = C^{-1}, \quad S = (4C)^{-1}(F^2 + 4NC - AC), \quad T = (2C)^{-1}(C - F). \tag{4}$$

Furthermore, we assume that the hypothetical isotropic equivalent is described in terms of the shear modulus μ and the squared S to P velocity ratio $\Theta = v_s^2/v_p^2$. Both μ and Θ must conform to the elastic stability conditions $\mu \geqslant 0$ and $0 \leqslant \Theta \leqslant 3/4$, which follow from the more general stability conditions (3). As shown in A, we can construct an isotropic equivalent composed of only two types of layers with constant Θ_1 and $\Theta_2 > \Theta_1$ if the inequalities

$$(\Theta_1 L^{-1} - R)(\Theta_1 N - S) - (\Theta_1 - T)^2 \geqslant 0, \quad \text{and}$$
$$(\Theta_2 L^{-1} - R)(\Theta_2 N - S) - (\Theta_2 - T)^2 \geqslant 0, \tag{5}$$

are satisfied simultaneously for $0 \leqslant \Theta_1 < T < \Theta_2 \leqslant 3/4$. The relation between μ and Θ and their long-wavelength equivalents L, N, R, S, and T is then

$$L = \langle \mu^{-1} \rangle^{-1}, \quad N = \langle \mu \rangle, \quad R = \langle \Theta \mu^{-1} \rangle, \quad S = \langle \Theta \mu \rangle, \quad T = \langle \Theta \rangle, \tag{6}$$

which follows from the combination of (2) and (4). The left-hand sides of the inequalities (5) are identical quadratic polynomials in Θ_1 and Θ_2, respectively. A finely layered isotropic equivalent therefore exists, when $(\Theta L^{-1} - R)(\Theta N - S) - (\Theta - T)^2$ is greater or equal to zero for a potentially small neighbourhood of Θ around T that falls within the stability range $0 \leqslant \Theta \leqslant 3/4$.

3.2. Examples

To illustrate the Backus conditions (5), we assume a fixed combination of $A = \rho v_{ph}^2, C = \rho v_{pv}^2$ and $\eta = F/(A - 2L)$, where the ratio η affects the azimuthal dependence of P and S velocities (e.g., Takeuchi and Saito, 1972; Dziewoński and Anderson, 1981). Then we determine the combinations of $N = \rho v_{sh}^2$ and $L = \rho v_{sv}^2$ for which a finely layered isotropic equivalent exists. Density cancels in the Backus conditions, meaning that the wave speeds $v_{ph}, v_{pv}, v_{sh}, v_{sv}$, and η fully determine stability, and the possible existence of an isotropic equivalent.

Fig. 2a shows an example where $v_{ph} = 8.10$ km/s, $v_{pv} = 7.90$ km/s and $\eta = 0.93$. The black region marks combinations of v_{sh} and v_{sv} for which the medium is unstable. Grey regions imply stability without the possibility of isotropic equivalence. The remaining coloured regions correspond to stability and the possible existence of a finely layered isotropic equivalent. The black diagonal line separates $v_{sh} > v_{sv}$ (right) from $v_{sh} < v_{sv}$ (left). Horizontal lines and colours indicate various ranges of $\Theta = v_s^2/v_p^2$ within the isotropic equivalent. Yellow, for instance, means that a finely layered isotropic equivalent exists – for a given combination of v_{sh} and v_{sv} – when Θ is allowed to range from 0.1 to 0.3 between the different layers. For the same v_{sh}-v_{sv} combination an isotropic equivalent still exists when this range is extended, say to $0 \leqslant \Theta \leqslant 0.4$. Values of $\Theta > 0.5$ correspond to auxetic materials, i.e., materials with negative Poisson ratio. Thus, white, yellow and orange mean that isotropic equivalents can exist without the need to invoke an auxetic rheology that is unrealistic for the Earth. Fig. 2a suggests that an isotropic equivalent can be found for $0.13 < \Theta < 0.75$ when $v_{sh} > v_{sv}$, at least for this specific set of v_{ph}, v_{pv} and η.

A reduction of v_{ph} by 1.2% combined with an increase of v_{pv} by 1.4%, leads to the example shown in Fig. 2b. An isotropic equivalent may now be found for $v_{sh} < v_{sv}$ when Θ ranges between 0 and 0.48, and for $v_{sh} > v_{sv}$ when $\Theta > 0.48$. Figs. 2c and d shows the

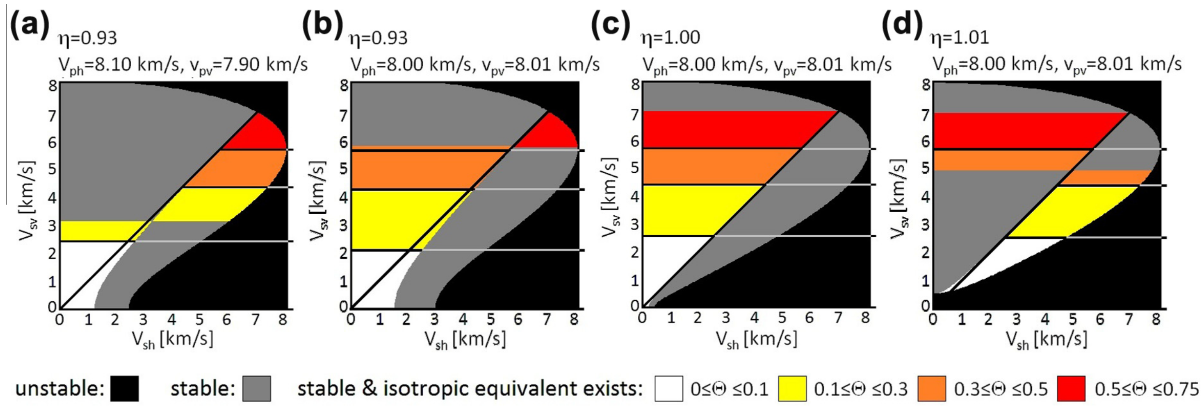

Fig. 2. Ranges of elastic stability and possible isotropic equivalence for various fixed combinations of $v_{\mathrm{ph}}, v_{\mathrm{pv}}$ and η. Black regions mark combinations of v_{sh} and v_{sv} that are elastically unstable. Grey indicates elastic stability. White, yellow, orange and red corresponds to pairs of v_{sh} and v_{sv} that are elastically stable, and for which a finely layered isotropic equivalent can be found for specific ranges of Θ. The diagonal black lines separate $v_{\mathrm{sh}} > v_{\mathrm{sv}}$ (right) and $v_{\mathrm{sh}} < v_{\mathrm{sv}}$ (left). Horizontal lines and colours separate various ranges of $\Theta = v_{\mathrm{s}}^2/v_{\mathrm{p}}^2$ in the isotropic equivalent. Values of $\Theta > 0.5$ correspond to auxetic materials, i.e., materials with negative Poisson ratio.

result of slight modifications in η. Note that an increase of η by 1% can completely change the combinations of v_{sh} and v_{sv} for which an isotropic equivalent can be found.

The examples in Fig. 2 suggest that $v_{\mathrm{ph}}, v_{\mathrm{pv}}$ and η must be known with considerable precision in order to determine whether observed anisotropy is – at least to some degree – intrinsic, or whether it may be explained fully by isotropic heterogeneity.

Examples similar to this one are possible for any other orientation of the symmetry axis, including a horizontal symmetry axis that is used in the analysis of SKS splitting.

3.3. Equivalence

We should stress that the long-wavelength averaging of the laminate isotropic structure is fully equivalent to the transverse isotropic representation. This applies to the variation of the wavespeeds with angle of propagation, and a necessary deviation of the group velocity associated with energy propagation from the phase velocity. Furthermore, surface wave dispersion will be equivalent, i.e., we will see Love and Rayleigh dispersion that appears to be incompatible with a simple medium that is smooth or composed of only few isotropic layers. The addition of complexity through lamination provides sufficient degrees of freedom to match the dispersion character with purely isotropic materials, though not in a simple way that could be used constructively in tomographic inversions that generally favour simplicity.

It is worth noting that such averaging properties as we have seen for elastic moduli will apply to the case of more general constitutive relations. Effective anisotropy can be induced in, e.g., rheological behaviour as the net effect of locally isotropic materials.

4. Perturbation analysis

To substantiate our conjecture that slight variations of elastic parameters can strongly perturb the regions of possible isotropic equivalence, we perform a perturbation analysis of the Backus conditions (5) that assumes small anisotropy and plausible Earth materials. First, we define the quadratic function $g(\Theta)$:

$$g(\Theta) = (\Theta L^{-1} - R)(\Theta N - S) - (\Theta - T)^2. \tag{7}$$

In terms of g, the Backus conditions (5) require that there exists at least a small neighbourhood around T for which $g(\Theta)$ is positive. This is illustrated in Fig. 3. Expanding g, yields

$$g(\Theta) = \Theta^2(NL^{-1} - 1) + \Theta(2T - SL^{-1} - RN) + RS - T^2. \tag{8}$$

Re-substituting the original elastic parameters L, N, A, C and F, gives

$$g(\Theta) = \Theta^2\left(\frac{N}{L} - 1\right) + \Theta\left[\frac{1}{C}(C-F) - \frac{1}{4CL}(F^2 + 4NC - AC) - \frac{N}{C}\right] + \frac{N}{C} - \frac{A}{4C} - \frac{1}{4} + \frac{F}{2C}. \tag{9}$$

In the next step we factorise $(CL)^{-1}$ from Eq. (9):

$$CLg(\Theta) = \Theta^2(NC - CL) + \Theta\left(CL - FL - \frac{1}{4}F^2 - NC + \frac{1}{4}AC - NL\right) + NL - \frac{1}{4}AL - \frac{1}{4}CL + \frac{1}{2}FL. \tag{10}$$

To study the case of weak anisotropy, we introduce the small parameters $\varepsilon_\eta, \varepsilon_A$ and ε_L, defined as

$$\eta = \frac{F}{A - 2L} = 1 + \varepsilon_\eta, \tag{11}$$

$$N = L + \varepsilon_L, \tag{12}$$

$$C = A + \varepsilon_A. \tag{13}$$

Thus, in the case of isotropy, we have $\varepsilon_\eta = 0, \varepsilon_L = 0$ and $\varepsilon_A = 0$. Substituting (11)–(13) into (10), and omitting all quadratic terms in the small quantities $\varepsilon_\eta,\ \varepsilon_A$ and ε_L, gives

$$CLg(\Theta) = \Theta^2(A\varepsilon_L) + \Theta\left[AL\varepsilon_\eta + A\left(\frac{1}{4}\varepsilon_A - \varepsilon_L\right) - L\varepsilon_L - \frac{1}{2}A^2\varepsilon_\eta\right] - L^2\varepsilon_\eta + L\left(\varepsilon_L - \frac{1}{4}\varepsilon_A\right) + \frac{1}{2}AL\varepsilon_\eta. \tag{14}$$

For further analysis, we make the reasonable assumption that physically plausible values for $\Theta = v_{\mathrm{s}}^2/v_{\mathrm{p}}^2$ may be found in the vicinity of $L/A = v_{sv}^2/v_{ph}^2$, i.e.

$$\Theta = \frac{L}{A} + \theta, \tag{15}$$

with θ being a small perturbation of Θ away from L/A. Inserting (15) into (14), and omitting quadratic terms in θ, gives

$$g\left(\frac{L}{A} + \theta\right) = \theta\left[\underbrace{\varepsilon_\eta}_{\mathcal{O}(10^{-2})}\underbrace{\frac{A}{C}}_{\approx 1}\underbrace{\left(1 - \frac{A}{2L}\right)}_{\approx -0.7} + \underbrace{\frac{\varepsilon_L}{L}}_{\mathcal{O}(10^{-2})}\underbrace{\frac{(L-A)}{C}}_{\approx -0.75} + \frac{1}{4}\underbrace{\frac{\varepsilon_A}{C}}_{\mathcal{O}(10^{-2})}\underbrace{\frac{A}{L}}_{\approx 1}\right], \tag{16}$$

where the numerical values below the curly brackets are for standard global Earth models (e.g., Dziewoński and Anderson, 1981;

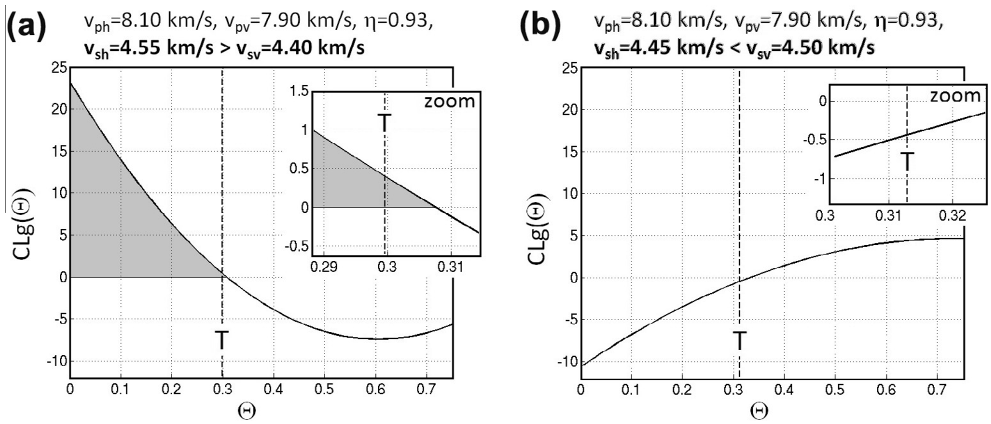

Fig. 3. Illustrations of the parabola $CLg(\Theta)$ as defined in Eq. (10), for two combinations of $v_{\rm ph}, v_{\rm pv}, \eta, v_{\rm sh}$ and $v_{\rm sv}$. (a) This parabola corresponds to the example from Fig. 2a for $v_{\rm sh} > v_{\rm sv}$. The grey-shaded area marks Θ values around $\Theta = T$ for which the parabola lies above zero. Since we can find Θ_1 and Θ_2 with $0 \leqslant \Theta_1 < T < \Theta_2 \leqslant 3/4$ and $g(\Theta_1) > 0$ and $g(\Theta_2) > 0$, an isotropic equivalent exists. A zoom into the parabola around $\Theta = T$ is shown to the left. (b) The same as above, but for $v_{\rm sh} < v_{\rm sv}$. There are no Θ values around $\Theta = T$ for which the parabola lies above zero. Therefore, an isotropic equivalent does not exist.

Kennett and Engdahl, 1991; Kennett et al., 1995) around 100 km depth and weak anisotropy. Eqs. (15) and (16) reveal that a zero of (14) is, correct to first order, located at $\Theta = L/A$. What controls the possible existence of an isotropic equivalent are the slope of (16) and the position of its zero at $\Theta = L/A$ relative to

$$T = \underbrace{\frac{L}{A}}_{\approx 1} - \underbrace{\varepsilon_\eta}_{\mathcal{O}(10^{-2})} \underbrace{\left(\frac{1}{2} - \frac{L}{A}\right)}_{\approx 0.2}, \tag{17}$$

which is also correct to first order. Numerical values below curly brackets are again for around 100 km depth and weak anisotropy. The slope of the line (16) is determined by the delicate interplay of comparatively large numbers of $\mathcal{O}(1)$, pre-multiplied by anisotropic perturbations ($\varepsilon_\eta, \varepsilon_L/L, \varepsilon_A/C$) that typically range around plus or minus a few percent. This implies that minor changes of anisotropic properties can strongly influence the slope of (16), thereby affecting the possible existence of an isotropic equivalent. Similarly, the position of the zero of (7) or (16) at $\Theta = L/A$ relative to T from Eq. (17) is controlled by the sign of ε_η. It follows that we cannot decide about the existence of an isotropic equivalent when the sign of $\varepsilon_\eta = \eta - 1$ is not known precisely, i.e., when the error bars around a tomographically estimated η include 1.

Eq. (16) explains the existence fields of isotropic equivalents observed in the examples from Fig. 2. Small variations in ε_L change the slope of the parabola $g(\Theta)$ in the vicinity of $\Theta = T$ from negative (for $v_{\rm sh} > v_{\rm sv}$) to positive (for $v_{\rm sh} < v_{\rm sv}$), thereby eliminating the possibility that the observed anisotropy can be explained by a purely isotropic equivalent.

5. Intrinsic vs. apparent anisotropy in the context of tomographic inversions

While anisotropy in the Earth is likely to be complicated, the limited resolving power of seismic data requires assumptions of unrealistically high symmetry to reduce the number of independent elastic parameters. The restriction to transverse isotropy falls into this class of simplifications. In mantle tomography, the number of independent elastic parameters is often further reduced from five to two (e.g., Panning and Romanowicz, 2006; Nettles and Dziewoński, 2008; Fichtner et al., 2010; Yoshizawa and Ekström, 2010). This reduction becomes necessary because P wave anisotropy (e.g., in terms of A and C) and η can hardly be constrained independently from seismic observables that are mostly sensitive to S wave anisotropy (e.g., $v_{\rm sh}$ and $v_{\rm sv}$). The specific way of treating P wave anisotropy and η leaves considerable freedom of choice that is to some degree subjective. Such choices affect the existence of isotropic equivalents.

The simplest, though mineralogically implausible, treatment of P wave anisotropy and η in tomographic inversions is to enforce P wave isotropy, i.e., $v_{\rm ph} = v_{\rm pv}$, and $\eta = 1$ (e.g., Debayle and Kennett, 2000; Fichtner et al., 2010; Yoshizawa and Ekström, 2010). Existence diagrams for isotropic equivalents at 100, 300 and 1000 km depth are shown in Fig. 4. The isotropic reference P and S velocities at the various depth levels are taken from the 1D model PREM (Dziewoński and Anderson, 1981). Fig. 4 reveals that models with $v_{\rm sh}$ and $v_{\rm sv}$ variations of up to ±10% around the reference $v_{\rm s}$ can always be represented by purely isotropic equivalents, without the need to invoke nearly fluid ($0 \leqslant \Theta \leqslant 0.1$) or auxetic ($\Theta \geqslant 0.5$) materials. The existence diagrams for isotropic equivalents from Fig. 4 can be incorporated in tomographic models to reveal where isotropic equivalents can exist and what their possible properties are. This is illustrated in Fig. 5 for the Australasian model of Fichtner et al., 2010 at 70 and 150 km depth. As predicted by the diagrams in Fig. 4, the radial anisotropy in the complete model can be explained by a finely layered isotropic equivalent. Isotropic layers with $\Theta = v_{\rm s}^2/v_{\rm p}^2$ well below 0.3 are needed beneath the Tasman and Coral Seas east of mainland Australia, as well as along the Phanerozoic eastern margin of the continent (yellow areas in Fig. 5). In contrast, isotropic layers with $\Theta = v_{\rm s}^2/v_{\rm p}^2$ well above 0.3 are needed beneath most of Precambrian central and western Australia in order to explain the observed radial anisotropy in terms of an isotropic stratification (orange areas in Fig. 5).

Alternative treatments of P wave anisotropy and η are based on empirical relations between elastic parameters for plausible mineral assemblages (Montagner and Anderson, 1989). For instance, a transversely isotropic material parameterised in terms of

$$v_{\rm s} = \sqrt{\frac{2}{3} v_{\rm sv}^2 + \frac{1}{3} v_{\rm sh}^2}, \quad v_{\rm p} = \sqrt{\frac{1}{5} v_{\rm pv}^2 + \frac{4}{5} v_{\rm ph}^2}, \quad \xi = \frac{v_{\rm sh}^2}{v_{\rm sv}^2}, \quad \phi = \frac{v_{\rm pv}^2}{v_{\rm ph}^2} \tag{18}$$

and η can effectively be described by the two S wave parameter perturbations $\delta v_{\rm s}$ and $\delta\xi$ when the empirical relations

$$\frac{\delta \ln v_{\rm p}}{\delta \ln v_{\rm s}} = 0.5, \quad \frac{\delta \ln \eta}{\delta \ln \xi} = -2.5, \quad \frac{\delta \ln \phi}{\delta \ln \xi} = -1.5 \tag{19}$$

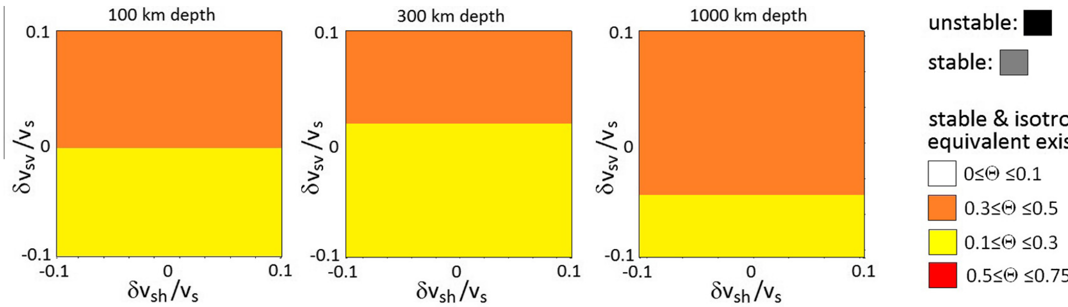

Fig. 4. Existence diagrams for isotropic equivalents at 100, 300 and 1000 km depth when P wave anisotropy is neglected ($v_{ph} = v_{pv}$) and η is set to 1. Shown are relative variations of v_{sh} and v_{sv}. Reference values are taken from the isotropic version of PREM (Dziewoński and Anderson, 1981). For variations of up to $\pm 10\%$ in v_{sh} and v_{sv}, the elastic medium is generally stable (no black fields). It can, furthermore, be represented by purely isotropic equivalents with Θ in the range from 0.1 to 0.5 (yellow and orange fields).

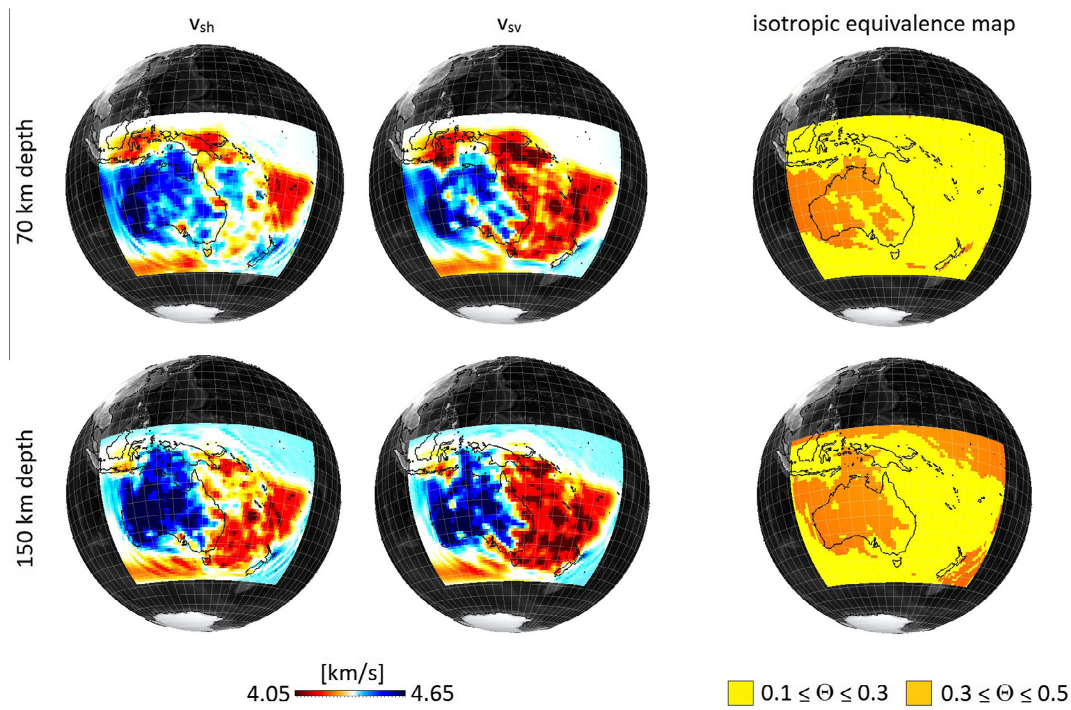

Fig. 5. Possible isotropic equivalence in a tomographic model. Left: horizontal slices at 70 and 150 km depth through the v_{sh} and v_{sv} distributions in the radially anisotropic model of Fichtner et al., 2010. In this model, P wave anisotropy is ignored, i.e., $v_{ph} = v_{pv}$, and $\eta = 1$. Right: corresponding existence maps for isotropic equivalents, using the same colour coding as in Fig. 4. Isotropic equivalents can express the radial anisotropy throughout the whole model, with a clear preference of layers with high $\Theta = v_s^2/v_p^2$ beneath Precambrian central and western Australia. Isotropic layers with Θ well below 0.3 are needed beneath the Tasman and Coral Seas east of Australia, as well as along the Phanerozoic eastern margin of the continent.

are enforced (e.g., Panning and Romanowicz, 2006; Marone et al., 2007). The corresponding existence diagrams of isotropic equivalents at 100, 300 and 1000 km depth are shown in Fig. 6, with reference values again taken from PREM (Dziewoński and Anderson, 1981). Within $\pm 10\%$ variations of χ and v_s, all models are elastically stable. Isotropic equivalents exist for wide ranges of $\delta\xi$-δv_s combinations that are strongly depth dependent without having an easily classifiable pattern. However, the empirical scaling relations (19) can produce transversely isotropic models for which a purely isotropic equivalent cannot be found (grey fields).

The comparison of Figs. 4 and 6 illustrates the effect of the rather subjective choice of coupling between P and S wave anisotropy. In accord with our results from Section 4, subtle changes in P wave anisotropy and η in particular, strongly influence the possible existence of isotropic equivalents.

6. Discussion

6.1. Inferences on anisotropy from SKS splitting

While our illustration in Section 5 is based on surface wave tomography, similar examples are possible for SKS splitting because both use the same mathematical model – transverse isotropy described by five elastic parameters (e.g., Silver and Chan, 1988; Babuška and Cara, 1991). Anisotropy inferred from SKS splitting is therefore naturally included in our analysis. Similar to surface wave tomography, SKS splitting does not constrain P wave anisotropy. Furthermore, inferred S wave anisotropy carries large uncertainties due to the lack of depth resolution. It follows, that SKS splitting is also not able to discriminate between intrinsic and apparent anisotropy.

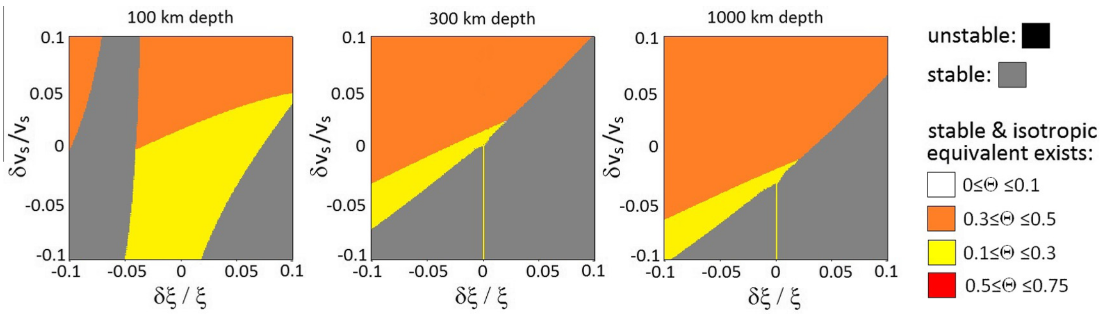

Fig. 6. Existence diagrams for isotropic equivalents at 100, 300 and 1000 km depth when P wave anisotropy and η are related to S wave anisotropy via the empirical scaling relations of Eq. (19) that were proposed by Montagner and Anderson (1989), and used, for instance by Panning and Romanowicz (2006) and Marone et al. (2007). Reference values at the various depth levels are taken from PREM (Dziewoński and Anderson, 1981). Isotropic equivalents exist for wide ranges of $\delta\xi$–δv_s combinations that are strongly depth dependent without having an easily classifyable pattern.

6.2. Existence of small-scale heterogeneity in the Earth

Wherever we have intermingled structures elongated transverse to the general direction of propagation of seismic waves, e.g., in the form of SPO, we can expect apparent anisotropy. Even when the materials are intrinsically anisotropic, the longer wavelength resultant will be apparent anisotropy, with characteristics different from those of the constituents. Do such classes of structures exist naturally within the Earth?

Indeed, we can recognise a number of examples related to the lithosphere–asthenosphere system. Within the crust, numerical modelling of coda waves provides evidence for a nearly self-similar distribution of heterogeneities across a wide range of length scales (Frankel, 1989). In many subduction zones, deep seismic events produce high-frequency waves that are efficiently transmitted to the surface to produce anomalously large ground motion concentrated on the land closest to the trench. Significant effects in eastern Japan are seen from events as deep as 500 km in the subducting Pacific plate. The ducting of these high frequency waves (up to 20 Hz) along the subduction zone can be achieved by a stochastic waveguide composed of a quasi-laminate structure with wavespeed variations of a few percent superimposed on the deterministic structure, with correlation lengths around 20 km downslab and 0.5 km across the slab thickness (Furumura and Kennett, 2005). Locally there are alternations of higher and lower wavespeed that encourage trapped propagation along the foliation, and which will impose apparent anisotropy in the subducted slab. A similar class of structure explains the very efficient propagation of high-frequency waves from the Indonesian subduction zone to northern Australia (Kennett and Furumura, 2008) through both oceanic and cratonic lithosphere, and also the propagation of high-frequency Po/So waves in the western Pacific to more than 3000 km from the source. Similar structures have been invoked in the interpretation of dense seismic profiles from peaceful nuclear explosions in the former Soviet Union (e.g., Morozova et al., 1999; Rydberg et al., 2000) though there are differences of opinion about how much of the observed effects arise at the base of the crust rather than in the lithospheric mantle (Nielsen et al., 2003). Other classes of observations indicate the need for complex structures in the lithospheric mantle with rapid wavespeed variations with depth below 100 km (Thybo and Perchuc, 1997). Based on observations of PKP precursors, Hedlin et al., 1997 suggest the presence of $\sim$ 10-km-scale heterogeneities throughout the mantle.

Inferences from receiver function studies from ocean bottom seismographs suggest the presence of a *mille-feuille* structure with elongate melt pockets (SPO) of similar dimensions to that proposed for lithospheric heterogeneity (Kawakatsu et al., 2009). Such structure will induce apparent anisotropy in both seismological and rheological properties.

Were the temperature in the asthenosphere to drop, one can envisage such a structure ‘freezing in’ to give a quasi-laminate. This process would provide one mechanism for adding heterogeneity to the base of the lithosphere as the oceanic plate cools moving away from the mid-ocean ridge, which could then be delivered to a subduction zone. The quasi-laminate nature of the older parts of the continental lithosphere would provide a significant contribution to the well recognised faster SH waves in the cratons (e.g., Gung et al., 2003; Fichtner et al., 2010; Kennett et al., 2013) without precluding intrinsic anisotropy for which there is independent evidence (e.g., Debayle and Kennett, 2000).

For a general intrinsically anisotropic medium we would expect comparable levels of azimuthal and polarisation anisotropy. Yet for cratons, at least, the estimates of polarisation anisotropy are much larger than for azimuthal anisotropy. For Australia, for instance, azimuthal anisotropy is around 2% (Fishwick et al., 2008) while polarisation anisotropy exceeds 5% (Fichtner et al., 2010). The contribution to apparent polarisation anisotropy from the quasi-laminate heterogeneity proposed by Kennett and Furumura (2008) would be around 3%, which is of a similar size to the discrepancy between azimuthal and polarisation anisotropy.

Current geodynamic models for the Earth favour a convective regime in the mantle with a high Rayleigh number, but also a low Reynolds number. In consequence we expect a scenario where mantle material is well-stirred, but where initially distinct components are not well mixed (e.g., Davies, 1999). Over time heterogeneity will tend to become more streaky, imposing a regime of small-scale heterogeneity with rapid variations in properties in some directions, but much slower change orthogonally. This is precisely the configuration that can be described by apparent anisotropy, on some scale. The net effect on global scales will depend on the degree of organisation of the inter-threading structures. The seismic wavelengths employed in global studies, and the regions they sample around the nominal propagation path, are most likely large enough to smear out the influences of streaky heterogeneity, and thus we see a mantle that cannot be distinguished from isotropic.

6.3. Constraints on P wave anisotropy

One of our principal conclusion is that P wave anisotropy must be known with considerable precision in order to assess the possible existence of isotropic equivalents. Although evidence has been presented in the context of seismic tomography for radial anisotropy in P waves (Boschi et al., 2000), it is difficult to justify the increase in the numbers of degrees of freedom in the model relative to the improvement in data fit. Direct evidence for P anisotropy is confined to the crust and the uppermost mantle (e.g., Fuchs, 1977; Schulte-Pelkum et al., 2001; Fontaine et al., 2009), and the results are quite sensitive to the presence of heterogeneity. It is therefore rather unlikely that it will be generally possible to extract P wavespeed parameters with the precision that would allow an unambiguous separation of intrinsic and apparent anisotropy, even in the simple case of transverse isotropy.

6.4. More complex forms of anisotropy

We restricted ourselves to transverse isotropy because the separation of intrinsic and apparent anisotropy can be studied analytically. The Earth is certainly not transversely isotropic, but macroscopically triclinic due to the presence of multiple mineral phases with different orientations and concentrations. More general cases of anisotropy could be analysed using the 3D version of non-periodic homogenisation (Capdeville et al., 2010b,a), but the complexity of this problem is daunting.

At this point we can only conjecture that the separation of intrinsic and apparent anisotropy becomes more difficult when the symmetry of the assumed elastic tensor is further reduced. Reducing symmetry introduces additional elastic parameters, some of which control P wave anisotropy. In the Earth's mantle, however, constraints on P wave anisotropy are weak. Thus, the number of uncertain parameters increases with decreasing symmetry. We would therefore expect that it effectively becomes easier to find small-scale isotropic models that are equivalent within the error bars to a given anisotropic model.

7. Conclusions

The flow of Earth materials leads to LPO of intrinsically anisotropic materials that produces observable seismic anisotropy. Assuming that all seismic anisotropy results from LPO, this link is frequently used to infer rheology and flow patterns from anisotropic tomographic models.

While LPO certainly exists, observed seismic anisotropy can also be mimicked by heterogeneity at length scales smaller than the wavelength, for instance in the form of SPO or a sequence of fine layers. The existence of sub-wavelength heterogeneity in the Earth is predicted by convection at high Rayleigh and low Reynolds numbers, and observationally confirmed by strongly scattered seismic waves and the incompatibility of large polarisation and small azimuthal anisotropy in various tomographic models. Small-scale heterogeneity produces apparent anisotropy that need not be related to rheology and flow patterns in the same way as intrinsic anisotropy induced by LPO. Quantitative interpretations of observed seismic anisotropy in terms of Earth properties therefore require a separation of its apparent and intrinsic contributions.

At present, the problem of separating intrinsic and apparent anisotropy is too complex to be dealt with in full generality. However, by restricting ourselves to transversely isotropic media, we can gain valuable insight that may serve as a future starting point for studies of more complicated scenarios, based for instance on non-periodic homogenisation techniques (Capdeville et al., 2010b,a). To further reduce the level of difficulty to a presently tractable level, we only ask, under which circumstances a given transversely isotropic model can be represented by a completely isotropic finely layered equivalent. In cases where this is possible, intrinsic anisotropy is – strictly speaking – not required, thereby eliminating any possibility to infer the amount of intrinsic anisotropy from seismic observations.

Our main conclusion is that observed seismic anisotropy can nearly always be explained by purely isotropic layering, unless all anisotropic parameters are known with unrealistic accuracy. Both, the examples in Section 3.2 and the perturbation analysis in Section 4 indicate that the parameter η plays a particular role for the possible existence of isotropic equivalents. Minute changes in η can switch between possible and impossible isotropic equivalence. However, η is poorly constrained. It follows that intrinsic anisotropy over tomographically resolvable length scales is never strictly required when reasonable error bars for anisotropic parameters are taken into account.

We explicity stress that our results do not negate the existence of intrinsic anisotropy in the Earth, which is well observed, e.g., in the form of LPO in ophiolites. However, we have demonstrated that many aspects of anisotropy can be mimicked by slightly more complex isotropic structures. Indeed a significant component of large-scale anisotropy is likely to be associated with the way that seismic waves average out the properties of fine-scale variability. In the 3D heterogeneous Earth it will be very difficult from seismological data alone to unambigously assign the true amount of intrinsic anisotropy that may be related to flow via LPO, and so estimates need to be treated with caution. Thus convective flow patterns and the strength of the flow cannot be quantified on the basis of anisotropic tomographic models alone, and further geodynamic constraints are required, e.g., from gravity and topography for the lithosphere (e.g., Simons et al., 2003; Kirby et al., 2006). In future studies, seismic anisotropy and mantle flow should be inverted jointly on the basis of both geodynamic and seismic data, and by using realistic flow models that incorporate the formation of small-scale heterogeneity in convection regimes at high Rayleigh and low Reynolds number. Observations of seismic wave scattering (e.g. Hedlin et al., 1997; Furumura and Kennett, 2005; Kennett and Furumura, 2008; Kaneshima and Helffrich, 2009) could be incorporated to estimate the contribution of small-scale heterogeneity to observed anisotropy.

In our analysis, we considered transversely isotropic media that do not perfectly represent the Earth which is certainly triclinic. Nevertheless, we were able to obtain valuable insight into the nature of the problem.

Acknowledgements

This manuscript has gone through many hands, and it would not have taken shape without the contribution and inspiration from many colleagues. In particular we would like to thank Moritz Bernauer, Yann Capdeville, Lorenzo Colli, Paul Cupillard, Jean-Paul Montagner and Nian Wang. The constructive comments of the editor George Helffrich and two anonymous reviewers helped to improve the manuscript. Andreas Fichtner was funded by The Netherlands Research Center for Integrated Solid Earth Sciences under project number ISES-MD.5.

Appendix A. Conditions for the existence of an isotropic equivalent

We give a slightly more detailed and illustrated version of the proof of the inequalities (5), first derived by Backus (1962). As a preparatory step, we note an important lemma that we will need later: there is a function $\mu \geqslant 0$ such that

$$\langle \mu^{-1} \rangle = X^{-1}, \quad \langle \mu \rangle = Y, \tag{A.1}$$

if and only if $X \leqslant Y$. To verify this statement, we first assume $\langle \mu^{-1} \rangle = X^{-1}$ and $\langle \mu \rangle = Y$. Invoking Schwarz's inequality, we have

$$1 = \langle 1 \rangle^2 = \langle \mu^{-1/2} \mu^{1/2} \rangle^2 \leqslant \langle \mu^{-1} \rangle \langle \mu \rangle = X^{-1} Y, \tag{A.2}$$

which proves part one of the lemma. The proof of the second half is constructive: we consider a layered medium that is partitioned into two fractions $\mathcal{P}_1$ and $\mathcal{P}_2$ with constant shear moduli μ_1 and μ_2. Without loss of generality we let $\mu_2 > \mu_1$. Our goal is to find p_1 and p_2 with $p_1 + p_2 = 1$ such that

$$X^{-1} = \mu_1^{-1}\int_{\mathcal{P}_1} w(\xi - z)\,d\xi + \mu_2^{-1}\int_{\mathcal{P}_2} w(\xi - z)\,d\xi$$
$$= p_1\mu_1^{-1} + p_2\mu_2^{-1}, \tag{A.3}$$

and

$$Y = \mu_1\int_{\mathcal{P}_1} w(\xi - z)\,d\xi + \mu_2\int_{\mathcal{P}_2} w(\xi - z)\,d\xi = p_1\mu_1 + p_2\mu_2. \tag{A.4}$$

Both p_1 and p_2 may depend on z, and this dependence is controlled by the width of the various layers. Solving for p_1 and p_2, gives

$$p_1 = \frac{\mu_2 - Y}{\mu_2 - \mu_1}, \quad p_2 = \frac{Y - \mu_1}{\mu_2 - \mu_1}, \tag{A.5}$$

which implies $\mu_1 < Y < \mu_2$. This inequality motivates the ansatz

$$\mu_1 = Y - \chi, \quad \mu_2 = Y + \chi, \tag{A.6}$$

where χ remains to be determined. It follows from (A.6) that $\mu_1\mu_2 = Y^2 - \chi^2$, and therefore, with a little bit of algebra:

$$X^{-1}\mu_1\mu_2 = p_1\mu_2 + p_2\mu_1 = \frac{\chi\mu_2}{\mu_2 - \mu_1} + \frac{\chi\mu_1}{\mu_2 - \mu_1} = \chi\frac{\mu_2 + \mu_1}{\mu_2 - \mu_1}$$
$$= Y = X^{-1}(Y^2 - \chi^2). \tag{A.7}$$

Rearranging (A.6) gives

$$\chi^2 = Y(Y - X). \tag{A.8}$$

It follows that $X \leqslant Y$ is a necessary condition for Eq. (A.8) to have a real-valued solution for χ. This concludes the proof.

To pursue our original goal, we assume that the STILWE parameters L, N, R, S and T are given, and from them, we wish to construct a finely layered, elastically stable and isotropic medium. For this we divide the medium in two fractions $\mathcal{P}_1$ and $\mathcal{P}_2$ where Θ takes the constant values Θ_1 and $\Theta_2 > \Theta_1$, respectively. This is shown in Fig. A.7a. The effective parameter T is then given by

$$T = \int w(\xi - z)\,\Theta(\xi)\,d\xi$$
$$= \Theta_1\int_{\mathcal{P}_1} w(\xi - z)\,d\xi + \Theta_2\int_{\mathcal{P}_2} w(\xi - z)\,d\xi$$
$$= p_1\Theta_1 + p_2\Theta_2, \tag{A.9a}$$

with $p_1 + p_2 = 1$. Note that T, p_1 and p_2 can still be position-dependent because the width of the individual layers is not specified. Within each of the layers with constant Θ we assume at least two sub-layers with constant μ. Furthermore, we impose that the average shear modulus within each layer of a specific fraction is the same, as illustrated in Fig. A.7b. We denote the shear modulus averages within the layers of a fraction by $\langle\mu\rangle_1$ and $\langle\mu\rangle_2$. For the effective parameter N we then find

$$N = p_1\langle\mu\rangle_1 + p_2\langle\mu\rangle_2. \tag{A.9b}$$

Eq. (A.9b) holds because the width of each layer is small compared to the width of the window w. The shear modulus μ within a layer can therefore be replaced by its average $\langle\mu\rangle_1$ or $\langle\mu\rangle_2$, depending on the association with one of the two fractions. For the remaining effective parameters we obtain

$$L^{-1} = p_1\langle\mu^{-1}\rangle_1 + p_2\langle\mu^{-1}\rangle_2, \tag{A.9c}$$
$$R = p_1\Theta_1\langle\mu^{-1}\rangle_1 + p_2\Theta_2\langle\mu^{-1}\rangle_2, \tag{A.9d}$$
$$S = p_1\Theta_1\langle\mu\rangle_1 + p_2\Theta_2\langle\mu\rangle_2, \tag{A.9e}$$

Using $p_1 + p_2 = 1$, we can solve Eq. (A.9a) for p_1 and p_2:

$$p_1 = \frac{T - \Theta_2}{\Theta_1 - \Theta_2}, \quad p_2 = \frac{T - \Theta_1}{\Theta_2 - \Theta_1}. \tag{A.10}$$

From (A.10) we obtain expressions for the fractional averages of μ and μ^{-1}:

$$\langle\mu\rangle_1 = \frac{\Theta_2 N - S}{\Theta_2 - T}, \quad \langle\mu^{-1}\rangle_1 = \frac{\Theta_2 L^{-1} - R}{\Theta_2 - T}, \tag{A.11a}$$

$$\langle\mu\rangle_2 = \frac{S - \Theta_1 N}{T - \Theta_1}, \quad \langle\mu^{-1}\rangle_2 = \frac{R - \Theta_1 L^{-1}}{T - \Theta_1}. \tag{A.11b}$$

Upon invoking the previously shown lemma, we obtain conditions for the existence of a function μ such that Eqs. (A.11) hold. These conditions are

$$(\Theta_2 L^{-1} - R)(\Theta_2 N - S) \;\geqslant\; (\Theta_2 - T)^2, \tag{A.12a}$$
$$(R - \Theta_1 L^{-1})(S - \Theta_1 N) \;\geqslant\; (T - \Theta_1)^2. \tag{A.12b}$$

Thus, if we can find Θ_1 and Θ_2 such that the inequalities (A.12) are satisfied, we can construct a finely layered isotropic medium that has the effective parameters L, N, R, S and T. A procedure for finding the shear modulus distribution of the finely layered medium, is given in the proof, but μ is only specified up to its average within each of the fractions. Of course, Θ_1 and Θ_2 must conform to condition $0 \leqslant \Theta_1 < T < \Theta_2 \leqslant 3/4$.

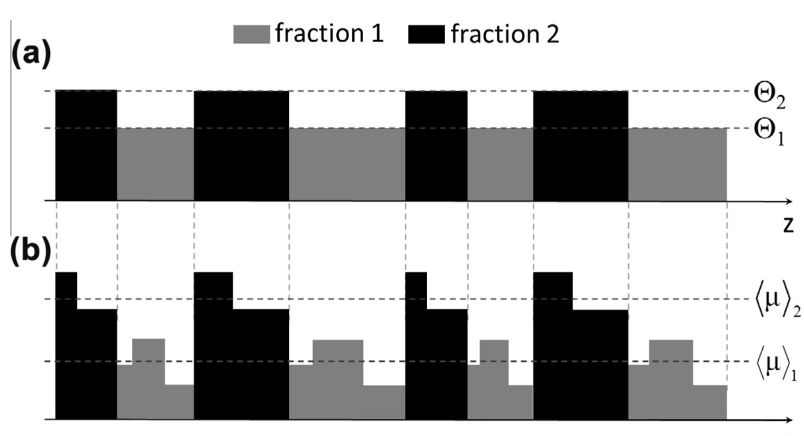

Fig. A.7. (a) Division of the layered medium into two fractions where $\Theta = v_s^2/v_p^2$ takes the constant values Θ_1 and $\Theta_2 > \Theta_1$, respectively. (b) The shear modulus distribution within each of the constant-Θ layers consists of at least two different types of sublayers. The average of μ over a constant-Θ layer – denoted $\langle\mu\rangle_1$ or $\langle\mu\rangle_2$ – is the same for each of the layers within a fraction. The widths of layers and sublayers is arbitrary and potentially variable as a function of z.

References

Turner, F.J., 1942. Preferred orientation of olivine crystals in peridotites, with special reference to New Zealand examples. Trans. R. Soc. N Z 72, 280–300.

Verma, R.K., 1960. Elasticity of some high-density crystals. J. Geophys. Res. 65, 757–766.

Hess, H.H., 1964. Seismic anisotropy of the uppermost mantle under oceans. Nature 203, 629–631.

Zhang, S., Karato, S.-I., 1996. Lattice preferred orientation of olivine aggregates deformed in simple shear. Nature 375, 774–777.

Mainprice, D., Tommasi, A., Couvy, H., Cordier, P., Frost, D.J., 2005. Pressure sensitivity of olivine slip systems and seismic anisotropy in the Earth's upper mantle. Nature 433, 731–733.

Raterron, P., Amiguet, E., Chen, J., Li, L., Cordier, P., 2009. Experimental deformation of olivine single crystals at mantle pressures and temperatures. Phys. Earth Planet. Int. 172, 74–83.

Ribe, N.M., 1989. Seismic anisotropy and mantle flow. J. Geophys. Res. 94, 4213–4223.

Chastel, Y.B., Dawson, P.R., 1993. Anisotropy convection with implications for the upper mantle. J. Geophys. Res. 98, 17757–17771.

Becker, T.W., Chevrot, S., Schulte-Pelkum, V., Blackman, D.K., 2006. Statistical properties of seismic anisotropy predicted by upper mantle geodynamic models. J. Geophys. Res. 111. http://dx.doi.org/10.1029/2005JB004095.

Becker, T.W., 2008. Azimuthal seismic anisotropy constrains net rotation of the lithosphere. Geophys. Res. Lett. 35. http://dx.doi.org/10.1029/2007GL032928.

Backus, G.E., 1962. Long-wave elastic anisotropy produced by horizontal layering. J. Geophys. Res. 67, 4427–4440.

Levshin, A., Ratnikova, L., 1984. Apparent anisotropy in inhomogeneous media. Geophys. J. R. Astr. Soc. 76, 65–69.

Babuška, V., Cara, M., 1991. Seismic Anisotropy in the Earth. Kluwer Academic Publishers, Dordrecht, Boston, London.

Fichtner, A., Igel, H., 2008. Efficient numerical surface wave propagation through the optimization of discrete crustal models – a technique based on non-linear dispersion curve matching (DCM). Geophys. J. Int. 173, 519–533.

Guillot, L., Capdeville, Y., Marigo, J.J., 2010. 2-D non periodic homogenization for the SH wave equation. Geophys. J. Int. 182, 1438–1454.

Capdeville, Y., Guillot, L., Marigo, J.J., 2010a. 2-D nonperiodic homogenization to upscale elastic media for P-SV waves. Geophys. J. Int. 182, 903–922.

Capdeville, Y., Stutzmann, E., Montagner, J.-P., Wang, N., in press. Residual homogenization for seismic forward and inverse problems in layered media. Geophys. J. Int. doi: 10.1093/gji/ggt102.

Blackman, D.K., Kendall, J.M., 1997. Sensitivity of teleseismic body waves to mineral texture and melt in the mantle beneath a mid-ocean ridge. Philos. Trans. R. Acad. 355, 217–231.

Crampin, S., Chastin, S., 2003. A review of shear wave splitting in the crack-critical crust. Geophys. J. Int. 155, 221–240.

Bastow, I.D., Pilidou, S., Kendall, J.M., Stuart, G.W., 2010. Melt-induced seismic anisotropy and magma-assisted rifting in Ethiopia: evidence from surface waves. Geochem. Geophys. Geosys. 11. http://dx.doi.org/10.1029/2010GC003036.

Montagner, J.P., Jobert, N., 1988. Vectorial tomography – II. Application to the Indian Ocean. Geophys. J. 94, 309–344.

Trampert, J., Woodhouse, J.H., 2003. Global anisotropic phase velocity maps for fundamental mode surface waves between 40 and 150 s. Geophys. J. Int. 154, 154–165.

Bozdağ, E., Trampert, J., 2008. On crustal corrections in surface wave tomography. Geophys. J. Int. 172, 1066–1082.

Ferreira, A.M.G., Woodhouse, J.H., Visser, K., Trampert, J., 2010. On the robustness of global radially anisotropic surface wave tomography. J. Geophys. Res. 115, 1029/2009JB006716.

Love, A.E.H., 1927. A Treatise on the Theory of Elasticity. Cambridge University Press, Cambride, UK.

Silver, P., Chan, W.W., 1988. Implications for continental structure and evolution from seismic anisotropy. Nature 335, 34–39.

Trampert, J., Fichtner, A., 2013. Global imaging of the Earth's deep interior: seismic constraints on (an)isotropy, density and attenuation. In: Karato, S. (Ed.), Physics and Chemistry of the Deep Earth. Wiley-Blackwell.

Takeuchi, H., Saito, M., 1972. Seismic Surface Waves. Methods Comput. Phys. 11, 217–295.

Dziewoński, A.M., Anderson, D.L., 1981. Preliminary reference Earth model. Phys. Earth Planet. Int. 25, 297–356.

Kennett, B.L.N., Engdahl, E.R., 1991. Traveltimes for global earthquake location and phase Identification. Geophys. J. Int. 105, 429–465.

Kennett, B.L.N., Engdahl, E.R., Buland, R., 1995. Constraints on seismic velocities in the Earth from traveltimes. Geophys. J. Int. 122, 108–124.

Panning, M., Romanowicz, B., 2006. A three-dimensional radially anisotropic model of shear velocity in the whole mantle. Geophys. J. Int. 167, 361–379.

Nettles, M., Dziewoński, A.M., 2008. Radially anisotropic shear velocity structure of the upper mantle globally and beneath North America. J. Geophys. Res. 113. http://dx.doi.org/10.1029/2006JB004819.

Fichtner, A., Kennett, B.L.N., Igel, H., Bunge, H.-P., 2010. Full waveform tomography for radially anisotropic structure: new insight into present and past states of the Australasian upper mantle. Earth Planet. Sci. Lett. 290, 270–280.

Yoshizawa, K., Ekström, G., 2010. Automated multimode phase speed measurements for high-resolution regional-scale tomography: application to North America. Geophys. J. Int. 183, 1538–1558.

Debayle, E., Kennett, B.L.N., 2000. Anisotropy in the Australasian upper mantle from Love and Rayleigh waveform inversion. Earth Planet. Sci. Lett. 184, 339–351.

Montagner, J.P., Anderson, D.L., 1989. Petrological constraints on seismic anisotropy. Phys. Earth Planet. Int. 54, 82–105.

Marone, F., Gung, Y., Romanowicz, B., 2007. Three-dimensional radial anisotropic structure of the North American upper mantle from inversion of surface waveform data. Geophys. J. Int. 171, 206–222.

Frankel, A., 1989. A review of numerical experiments on seismic wave scattering. Pure Appl. Geophys. 4, 639–685.

Furumura, T., Kennett, B.L.N., 2005. Subduction zone guided waves and the heterogeneity structure of the subducted plate – intensity anomalies in northern Japan. J. Geophys. Res. 110, 10.129/2004JB003486.

Kennett, B.L.N., Furumura, T., 2008. Stochastic waveguide in the lithosphere: Indonesian subduction zone to Australian craton. Geophys. J. Int. 172, 363–382.

Morozova, E.A., Morozov, I.B., Smithson, S.B., Solodilov, L.N., 1999. Heterogeneity of the uppermost mantle beneath Russian Eurasia from the ultra-long profile QUARTZ. J. Geophys. Res. 104, 20329–20348.

Rydberg, T., Tittgemeyer, M., Wenzel, F., 2000. Finite-difference modelling of P-wave scattering in the upper mantle. Geophys. J. Int. 141, 787–800.

Nielsen, L., Thybo, H., Levander, A., Solodilov, N., 2003. Origin of upper mantle seismic scattering – evidence from Russian peaceful nuclear explosion data. Geophys. J. Int. 154, 196–204.

Thybo, H., Perchuc, E., 1997. The seismic 8° discontinuity and partial melting in the continental mantle. Science 275, 1626–1629.

Hedlin, M.A.H., Shearer, P.M., Earle, P.S., 1997. Seismic evidence for small-scale heterogeneity throughout the Earth's mantle. Nature 387 (number6629), 145–150.

Kawakatsu, H., Kumar, P., Takei, Y., Shinohara, M., Kanazawa, T., Araki, E., Suyehiro, K., 2009. Seismic evidence for sharp lithosphere–asthenosphere boundaries of oceanic plates. Science 324, 499–502.

Gung, Y.C., Panning, M., Romanowicz, B., 2003. Global anisotropy and the thickness of continents. Geophys. J. Int. 422, 707–711.

Kennett, B.L.N., Fichtner, A., Fishwick, S., Yoshizawa, K., 2013. Australian Seismological Reference Model (AuSREM): mantle component. Geophys. J. Int. 192, 871–887.

Fishwick, S., Heintz, M., Kennett, B.L.N., Reading, A.M., Yoshizawa, K., 2008. Steps in lithospheric thickness within eastern Australia, evidence from surface wave tomography. Tectonics 27. http://dx.doi.org/10.1029/2007TC002116.

Davies, G.F., 1999. Dynamic Earth. Cambridge University Press.

Boschi, L., Dziewoński, A.M., 2000. Whole Earth tomography for delay times of P, PcP and PKP phases: lateral heterogeneities in the outer core or radial anisotropy in the mantle? J. Geophys. Res. 105, 13675–13696.

Fuchs, K., 1977. Seismic anisotropy of the subcrustal lithosphere as evidence for dynamical processes in the upper mantle. Geophys. J. R. Astr. Soc. 49, 167–179.

Schulte-Pelkum, V., Masters, G., Shearer, P.M., 2001. Upper mantle anisotropy from long-period P polarization. J. Geophys. Res. 154, 21917–21934.

Fontaine, F., Barruol, G., Kennett, B.L.N., Bokelmann, G.H.R., Reymond, D., 2009. Upper mantle anisotropy beneath Australia and Tahiti from P polarization: implications for real-time earthquake location. J. Geophys. Res. 114. http://dx.doi.org/10.1029/2008JB005709.

Capdeville, Y., Guillot, L., Marigo, J.J., 2010b. 1-D non periodic homogenization for the wave equation. Geophys. J. Int. 181, 897–910.

Simons, F.J., van der Hilst, R.D., Zuber, M.T., 2003. Seismic and mechanical anisotropy and the past and present deformation of the Australian lithosphere. Earth Planet. Sci. Lett. 211, 271–286.

Kirby, J.F., Swain, C.J., 2006. Mapping the mechanical anisotropy of the lithosphere using a 2D wavelet coherence, and its application to Australia. Phys. Earth Planet. Sci. Lett. 158, 122–138.

Kaneshima, S., Helffrich, G., 2009. Lower mantle scattering profiles and fabric below Pacific subduction zones. Earth Planet. Sci. Lett. 282, 234–239.